Title

Zn 2 SbN 3 : growth and characterization of a metastable photoactive semiconductor

Journal

Materials Horizons, 6(8)

ISSN

2051-6347

Authors

Arca, Elisabetta
Perkins, John D
Lany, Stephan
et al.

Publication Date

2019-09-16

DOI

10.1039/c9mh00369j

Peer reviewed

Zn_2SbN_3: Growth and Characterization of a Metastable Photoactive Semiconductor

Elisabetta Arca,[1]* John D. Perkins,[1] Stephan Lany,[1] Allison Mis[1,2], Bor-Rong Chen,[3] Patricia Dippo,[1] Jonathan L. Partridge,[1,4] Wenhao Sun,[5] Aaron Holder,[1,6] Adele C. Tamboli,[1] Michael F. Toney,[3,7] Laura T. Schelhas,[7] Gerbrand Ceder,[5,8] William Tumas,[1] Glenn Teeter,[1] and Andriy Zakutayev[1]*

[1] Materials Science Center, National Renewable Energy Laboratory, Golden, Colorado 80401, USA

[2] Department of Metallurgical and Materials Engineering, Colorado School of Mines, Golden, Colorado 80401, USA

[3] Stanford Synchrotron Light Source, SLAC National Accelerator Laboratory, Menlo Park, California 94025, USA

[4] Department of Chemistry and Biochemistry, The University of Texas at Austin, Austin, Texas 78705, USA

[5] Materials Science Division, Lawrence Berkeley National Laboratory, Berkeley, California 94720, USA

[6] Department of Chemical and Biological Engineering, University of Colorado Boulder, Boulder, Colorado 80309, USA

[7] Applied Energy Programs, SLAC National Accelerator Laboratory, Menlo Park, California 94025, USA

[8] Department of Materials Science and Engineering, University of California Berkeley, Berkeley, California 94720, USA

*Corresponding authors: Elisabetta.Arca@nrel.gov, Andriy.Zakutayev@nrel.gov

Abstract

Ternary nitride semiconductors with wurtzite-derived crystal structure is an emerging class of materials for optoelectronic applications compatible with GaN and related III-V compounds. In particular, II-IV-V_2 materials such as $ZnSnN_2$ and $ZnGeN_2$ have been very actively studied for applications in photovoltaic and light emitting devices. However, many other possible wurtzite-derived ternary nitrides have not been reported, and hence their optical and electrical properties remain unknown. Here, we report on Zn_2SbN_3 - the first Sb-based nitride and a photoactive semiconductor. Surprisingly, Zn_2SbN_3 contains Sb in the highest (+5) oxidation state with unusual tetrahedral coordination. This new Zn_2SbN_3 material has a solar-matched 1.6-1.7 eV band gap and shows near-band-edge room-temperature photoluminescence, demonstrating its promise as an optoelectronic semiconductor. Finally, Zn_2SbN_3 can be synthesized at low temperature in a wide range of processing conditions, despite being metastable according to theoretical calculations. All these results, as well as the band position measurements, indicate that Zn_2SbN_3 is a promising emerging semiconductor for applications as an absorber in photovoltaic and photoelectrochemical solar cells.

Keywords:

Ternary nitrides, combinatorial sputtering, solar absorber, zinc antimony nitride

Introduction.

Wurtzite-based ternary nitrides have been widely studied in recent years as potential replacements for costly III-V materials for optoelectronic applications. Members of the original family of $II-IV-N_2$ - such as $ZnSnN_2$, $ZnGeN_2$, and $ZnSiN_2$ - arose as structural analogs to III–V materials, where the group III element is replaced by a combination of elements from the adjacent groups.[1] Among these, $ZnSnN_2$ received substantial attention for its potential to overcome the miscibility gap present in traditional III-Vs that leads to the possibility of tuning the bandgap by controlling the disorder on the cation sublattice and the ratio between the two cations (Zn and Sn).[2, 3] Control of the carrier concentration has been challenging, and only recently have photovoltaic (PV) devices based on this material been demonstrated.[4] Recently, we showed that the family of wurtzite-derived materials - also known as tetrahedrally bonded nitrides - extends far beyond the II-IV-N_2 stoichiometry to include II_3-VI-N_4 and II_2-V-N_3 stoichiometries (with VI and V being transition metal or main group elements).[5, 6]

Most of the cations in the periodic table have been reported to form nitrides in either monometallic or bimetallic compounds[7-10]. To date, an exception to this rule is represented by antimony (Sb). Among the binaries Sb-nitrides predicted, both SbN[11] and Sb_3N[12] were only realized in amorphous thin-film form.[13, 14] Despite having a relatively high electronegativity (EN = 1.9), synthesis challenges arise because Sb tends to react quickly with any residual moisture or oxygen present in the growth environment to form amorphous oxynitrides. Regarding crystalline Sb-based ternary nitrides, the ICDD database reports only mixed-anion anti-perovskite antimonide-

nitrides, i.e., compounds having M-Sb-N stoichiometry (M being a metal, Sb being in the –3 oxidation state). Examples of these compounds include Mn_3SbN[15, 16] or those formed with alkaline-earth metals such as AE_3SbN,[16-18] where AE is Mg, Ca, Sr, or Ba. Theoretical predictions also exist for $BSb_{1-x}N_x$ alloys,[19] where the identical electronegativity of B and Sb would likely lead to strongly covalent semiconductors. As a result, to date, there is no experimental evidence of crystalline nitrides where Sb functions as a cation (positive oxidation state). In this paper, we present the synthesis and characterization of the functional properties of Zn_2SbN_3, the first ternary antimony nitride.

Results and Discussion.

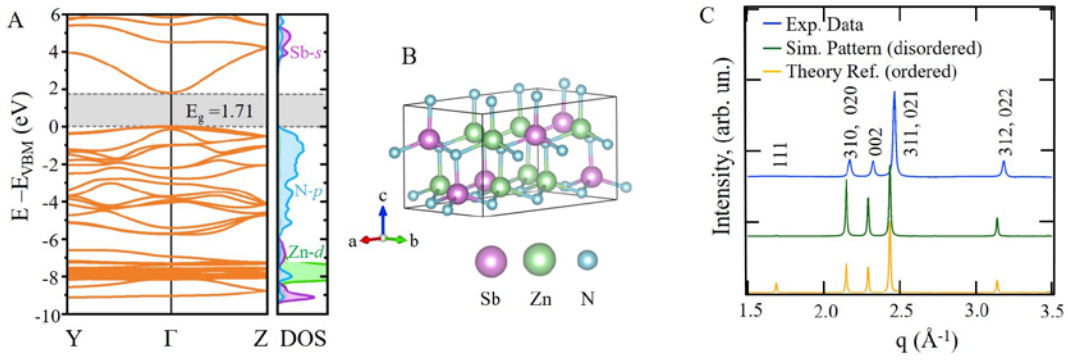

Figure 1. A) Band-structure calculations of the Zn_2SbN_3 phase and B) its crystal structure; C) Experimental X-Ray Diffraction pattern for a composition of f_{Zn} = 0.68 compared to the theoretical reference.

High-throughput calculations have identified Zn_2SbN_3 as a possible interesting chemical semiconductor.[6] The Zn_2SbN_3 phase is metastable and requires a minimum $\Delta\mu_N \geq +0.5$ eV above the nitrogen gas chemical potential, which has previously been

shown to be within range of non-equilibrium growth methods, such as reactive magnetron sputtering (Fig. SI1). The calculated band structure for the wurtzite-derived orthorhombic ground-state structure (SG 36, Figure 1B) is shown in Figure 1A, and it reveals compelling properties for optoelectronic applications.

The fundamental bandgap is 1.71 eV and is direct at the Γ point. The electron effective mass is anisotropic and very low in both directions: 0.15 m_e and 0.19 m_e parallel and perpendicular, respectively, to the wurtzite-derived equivalent c-axis. These low values are a consequence of the concave shape of the conduction band minimum, which results in highly dispersed bands. The density-of-states hole effective mass is 2.4 m_e, which is very close to the value calculated for GaN.[20]

We performed synthetic exploration of this chemical system using combinatorial sputtering from Zn and Sb targets on Eagle XG glass. Details of the growth conditions are reported in SI2. In line with the theoretical stability phase diagram (Figure SI1), the wurtzite-derived crystal structure shows stability over a wide composition region from f_{Zn} ~0.8 to ~0.5, with f_{Zn} being the Zn cation fraction Zn/(Zn+Sb). Films crystallize in the wurtzite-derived structure even when no heat is intentionally supplied during the growth and up to 300°C (Figure SI2). To ensure purity of the phase, we performed synchrotron-based X-Ray Diffraction (XRD) on selected spots of the combinatorial libraries. An example is given in Figure 1C for a stoichiometry of f_{Zn} = 0.68 as determined by X-Ray Fluorescence (XRF). All peaks present in the XRD pattern can be indexed to those of Zn_2SbN_3 in the wurtzite-derived structure. The XRD pattern simulated for the orthorhombic ground state of Zn_2SnN_3 ("theory ref." in Figure 1C) shows additional peaks - most notably, the (111) reflection that has zero intensity in

ideal wurtzite- that originate from ordering in the cation sublattice. The absence of these features in the experimental diffraction indicates that these films are cation disordered (disorder-simulated pattern in Figure 1C), although a high degree of short-range order is nevertheless possible.[21] The diffraction peaks are sharp and intense, indicating large diffraction domains. A small shift to larger q, corresponding to smaller unit cell, is observed, possibly caused by strain build into the film during deposition, or variation in stoichiometry for example due oxygen impurities.

XRF is not suitable for measuring light elements such as N, so the full stoichiometry was determined by Rutherford Back Scattering (RBS) for several points across the deposited sample library (Table SI1). For a composition of $f_{Zn} = 0.65$ as determined by XRF, the complete composition (determined by RBS) is $Zn_{1.7}SbN_3$. Oxygen contamination was present in these films in a low concentration (8.5% on the anion site) as shown in Table SI1. Thus, compositional and structural characterization confirmed the existence of the theoretically predicted Zn_2SbN_3 phase in the wurtzite-derived structure.

It is interesting to note that based on formal electron counting,[22] Sb is in its highest oxidation state, +5, and it is tetrahedrally coordinated. Fourfold coordination is rather uncommon for Sb (+5), which is most often encountered in octahedral coordination; this is in contrast to Sb (+3), for which tetrahedral coordination is very common.[23, 24]

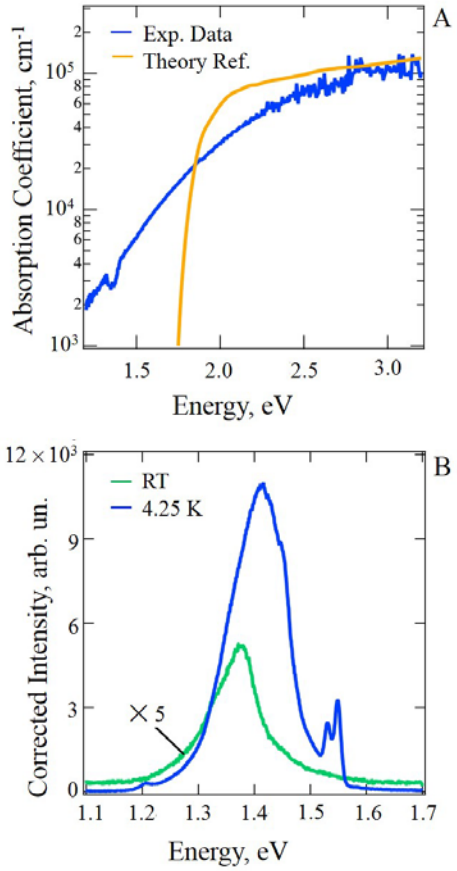

Figure 2. A) Comparison between the theoretically calculated and experimentally measured absorption coefficient for a Zn_2SbN_3 film. B) Photoluminescence (PL) measurements done on a stoichiometric film at low and room temperature (RT), respectively. The RT PL spectrum was magnified by a factor of 5 to compare it with the spectrum acquired at low temperature.

X-ray Photoelectron Spectroscopy (XPS) was performed on a film grown at room temperature to assess its chemical state at the surface (Figure SI3). To this end, a small portion of the sample, having composition f_{Zn} = 0.65±0.02, was cut out from the combinatorial library and loaded into the XPS instrument. The Zn $2p_{3/2}$ and Sb $3d_{5/2}$ core levels are positioned at 1021.6 eV and 530.5 eV, respectively. These binding

energies are comparable to those observed for the same core levels in other Zn-Sb compounds where Sb is present in the +5 oxidation state.[25-27] Additional bulk-sensitive measurements would be required to confirm these results obtained using a surface-sensitive technique.

Optical properties were characterized by UV-Visible spectroscopy (UV-Vis) and photoluminescence (PL) measurements. The experimental absorption coefficient determined by UV-Vis is reported in Figure 2A as well as the value predicted theoretically according to Density Functional Theory (DFT) calculations. The experimental and theoretical data agree in terms of the overall intensity of the absorption coefficient. GW-corrected DFT calculations predict the fundamental bandgap to be 1.71 eV with a very steep absorption onset, which compares to a more gradual onset around 1.4 –1.5 eV from experimentally measured UV-Vis spectroscopy (Figure 2A and Figure SI4). This discrepancy could originate from cation disorder and off-stoichiometry, which could cause Urbach-like tail states.[21]

PL emission was observed in these films at both low temperature (LT) and room temperature (RT). Figure 2B shows PL emission recorded at 4.25 K and RT using an excitation wavelength of 632.8 nm at 10-mW power for a small portion of the library grown at 300°C and having a composition $f_{Zn} = 0.68$. The LT measurements show a sharp peak at higher energy (1.55 eV) and a much broader peak at lower energy (1.4 eV). These PL features are similar to those observed in $ZnSnN_2$, where a more detailed analysis has shown that the broad feature is likely defect-related and the sharp feature is excitonic emission close to the fundamental bandgap.[3] Therefore, we tentatively assign the higher-energy feature to bound-exciton emission, which would place the

bandgap at about 1.55 eV - noting that this bandgap may deviate slightly from ideal Zn_2SbN_3 due to disorder and O incorporation.

It is quite remarkable to observe this sharp near-gap excitonic PL despite the tail present in the absorption data. To confirm the attribution of this PL activity to the Zn_2SbN_3 phase, we performed Transmission Electron Microscopy (TEM) analysis and Energy-Dispersive X-ray spectroscopy mapping (EDX) (Figure SI5). Both confirm that the material is polycrystalline, with no presence of secondary phases, and elements are homogeneously distributed across the probed area. This demonstrates that Zn_2SbN_3 is a photoactive material.

Resistance vs temperature measurements were performed on several samples, with an example reported in Figure SI6. The temperature-activated resistivity confirms that Zn_2SbN_3 has semiconducting behavior. Hall measurements were performed on a small portion of a library grown at 300°C and having f_{Zn} = 0.64 at RT. A Hall voltage of -2.9 cm^3C^{-1} was measured, indicating that the material is an n-type semiconductor. The mobility of the sample was measured to be 0.1 $cm^2V^{-1}s^{-1}$ with a carrier concentration of 2×10^{18} cm^{-3}, a value already suitable for optoelectronic applications. Based on theoretical studies carried out on similar wurtzite compounds such as $ZnSnN_2$ and $ZnGeN_2$, oxygen incorporation could be a possible source of n-type carriers, when present in dilute concentrations[28, 29]. Additional theoretical studies to understand the defect chemistry of Zn_2SbN_3 would be required to conclusively determine the nature of the intrinsic defects and assess their role in the observed n-type conductivity.

Scattering at defect centers and at grain boundaries can explain the observed low electron mobility in Zn_2SbN_3 thin films reported here, despite the very low theoretical

effective mass predicted for this material. Density of defects that are present in thin films sputtered on glass can be reduced by improving the crystal quality of the material, leading to a large improvement in the mobility. Recently this has been demonstrated for Mg-based nitrides such as $MgZrN_2$, for which mobility was improved by more than an order of magnitude using the templating effect of epitaxial substrates[30, 31]. Similar epitaxial methods or alternative growth techniques can be envisioned to reduce the defect density and improve the electron mobility in Zn_2SbN_3.

Optical and electrical properties of Zn_2SbN_3 were characterized as a function of composition within the crystalline range ($65 \leq f_{Zn} \leq 80$). Electrical properties vary substantially over this compositional range, with the material becoming completely insulating toward the two extremes of Zn-rich or Sb-rich values (Figure SI7). Contrary to many other wurtzite-derived nitrides, the optical absorption onset remains almost constant in the compositional range tested. This means that additional tuning of the carrier concentration might be possible by controlling the cation ratio.

To fully assess the potential of Zn_2SbN_3 as photoactive material, we performed XPS and ultraviolet photoelectron spectroscopy (UPS). A sample library was grown without intentional substrate heating at 20 mTorr and small piece of it, having composition f_{Zn} = 0.65±0.02, was cut out and loaded into the XPS system (Figure 3). This composition was chosen to correspond to the highest conductivity to facilitate the measurements. Air-free transfer was not possible for this sample, thus the quantities reported below are valid for air-exposed films. The position of the valence band maximum (VBM) is 1.3±0.05 eV below the Fermi level. This indicates a moderately n-type material, in good agreement with the electrical measurements. UPS measurements were performed

to determine the material work function and thus its ionization potential, which were found to be 4.2 eV and 5.5 eV, respectively (Figure 3). The electron affinity (EA) is then determined by summing the bandgap value. Depending on whether we use the experimental bandgap determined by PL (1.55 eV) or the theoretical value (1.71 eV), the EA is found to be 3.95 eV or 3.79 eV, respectively.

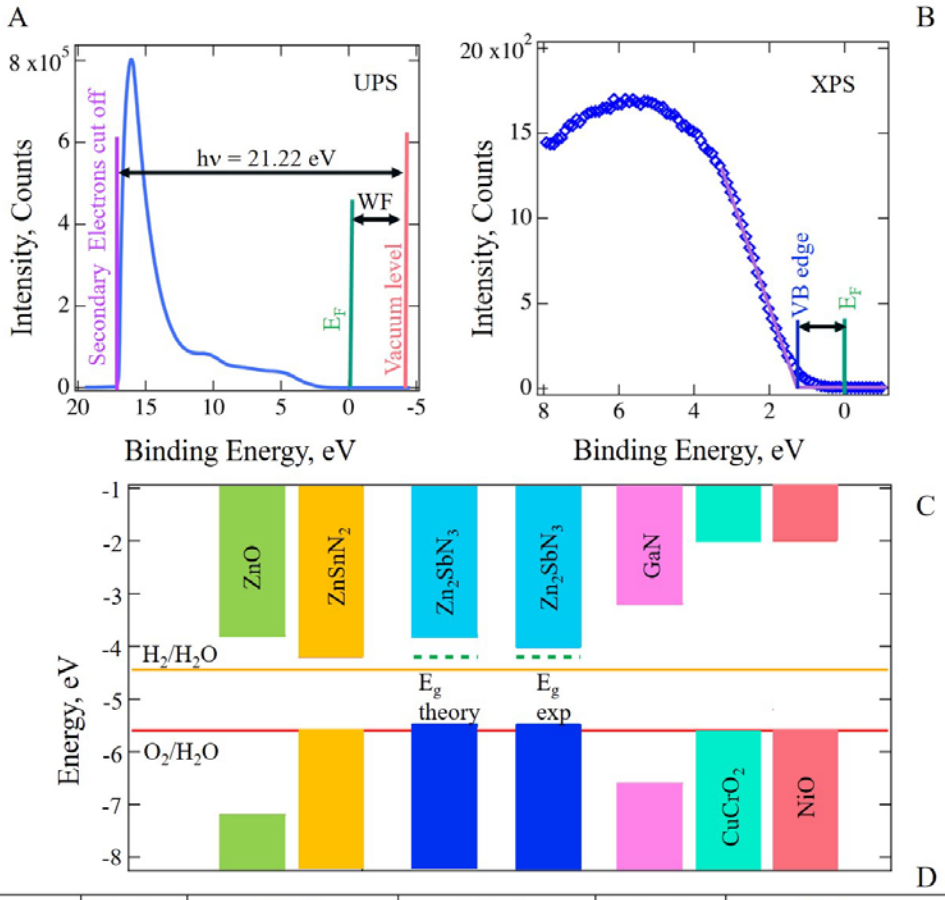

Mobility	Carrier Conc.	Effective mass	Band Gap	Ionization Potential	Electron Affinity	Work Function
0.1 $cm^2V^{-1}s^{-1}$	2×10^{18} cm^{-3}	μ_e = 0.15 - 0.19 m_e μ_h = 2.4 m_e	1.55 eV (PL) 1.71 eV (Theory)	5.5 eV	3.95 eV (Exp E_g) 3.79 eV (Theor. E_g)	4.2 eV

Figure 3. A) Work function (WF) determined by UPS measurements on a sample grown at RT and having composition f_{Zn} = 0.65±0.02; B) VBM measured by XPS. C) Vacuum-level alignment for the Zn_2SbN_3 sample measured in this work. Comparison to other

materials have been taken from Ref. [32]; D) Summary table of the optoelectronic properties of Zn_2SbN_3.

The low effective masses, moderate n-type conductivity, and observed RT photoluminescence (Figure 3D) make this material compelling for further exploration as a solar absorber. In particular, the 1.71-eV bandgap predicted by theory is ideal for a two-junction solar cell using a silicon bottom cell. With respect to other wurtzite-derived nitrides such as $ZnSnN_2$ that have been studied as PV absorbers, Zn_2SbN_3 has the advantage of having carrier concentration already suitable for implementing it in PV devices in its as-deposited form, without needing post-annealing treatments to reduce the native carrier concentrations.[33-35] Suitable junction partners would include traditional p-type transparent conducting oxides, such as $CuCrO_2$ or NiO, whereas GaN appears to be unsuitable because of the expected large valence-band offset. The position of the Zn_2SbN_3 VBM is relatively high, and the low native carrier concentration might make this material more prone to p-type doping using extrinsic impurities than similar nitrides such as $ZnSnN_2$.[36] Furthermore, based on the position of the conduction band minimum with respect to the H_2/H_2O level, this material is worth further investigation for Hydrogen Evolution Reactions (HERs) in water splitting. The suitability of nitrides for water-splitting applications has often been questioned because of nitrides' thermodynamic instability under the corrosive conditions used for HER. However, it was recently demonstrated that surface engineering and controlling the termination of carefully grown nanowires can allow GaN to perform in photoelectrochemical devices for hundreds of hours, despite its well-known thermodynamic instability in the acidic environment used.[37, 38] Regarding the

Oxygen Evolution Reactions (OERs), the VBM is only 0.1 eV higher than the O_2/H_2O potentials. In principle, this material could also be investigated for O_2/H_2O; however, its suitability as an OER largely depends on whether there is downward band-bending of the valence band upon exposure of the materials to the pH = 0 solution, which is a phenomenon often observed.[37]

Conclusions.

In conclusion, we grew and characterized Zn_2SbN_3, the first-ever- reported Sb-based nitride semiconductor and a new metastable ternary nitride. This material presents highly interesting properties such as the high +5 oxidation state of Sb, coupled with an unusual tetrahedral coordination environment. From an application standpoint, this semiconductor presents compelling functionalities: a direct theoretical bandgap of 1.71 eV (experimental 1.55 eV), carrier concentrations in the range suitable for device applications, and room-temperature photoluminescence. All these properties make Zn_2SbN_3 worth further investigation as a PV absorber and for HERs in water splitting.

Author contributions

E.A. and A. Z. conceived the idea, supervised experiments, and drafted the manuscript. E. A. prepared and characterized samples; J. D. P. carried out the RBS measurements; S. L., W.S., A.H. and G.C. performed the theoretical studies, A. M. carried out TEM measurements; B.-R.C., M.F.T and L.T.S performed the XRD synchrotron experiments, P. D. and A.C.T. performed and analyzed the PL measurements, J.L.P. performed the UV-Vis measurements under the supervision of E.A. and A.Z.; W.T.

oversaw the overall EFRC project, E.A. and G. T. performed the XPS experiments. All co-author reviewed the manuscript.

Conflicts of interest

The authors declare no conflict of interests.

Acknowledgements

This work was supported by the U.S. Department of Energy (DOE) under Contract No. DE-AC36-08GO28308 with Alliance for Sustainable Energy, LLC, the Manager and Operator of the National Renewable Energy Laboratory. Funding provided by Office of Science, Office of Basic Energy Sciences, as part of the Energy Frontier Research Center "Center for Next Generation of Materials Design: Incorporating Metastability." High-performance computing resources were sponsored by the DOE, Office of Energy Efficiency and Renewable Energy. A.T. was supported by DOE, Office of Science, Basic Energy Sciences, Materials Sciences and Engineering Division. A.M. was supported by a CoorsTek Fellowship through the Colorado School of Mines Foundation. Use of the Stanford Synchrotron Radiation Lightsource, SLAC National Accelerator Laboratory, was supported by the DOE, Office of Basic Energy Sciences, under Contract No. DE-AC02-76SF00515. The views expressed in the article do not necessarily represent the views of the DOE or the U.S. Government.

References

1. A. D. Martinez, A. N. Fioretti, E. S. Toberer and A. C. Tamboli, *J. Mater. Chem. A*, 2017, **5**, 11418-11435
2. T. D. Veal, N. Feldberg, N. F. Quackenbush, W. M. Linhart, D. O. Scanlon, L. F. J. Piper and S. M. Durbin, *Advanced Energy Materials*, 2015, **5**, 1501462.
3. A. N. Fioretti, J. Pan, B. R. Ortiz, C. L. Melamed, P. C. Dippo, L. T. Schelhas, J. D. Perkins, D. Kuciauskas, S. Lany, A. Zakutayev, E. S. Toberer and A. C. Tamboli, *Materials Horizons*, 2018, **5**, 823-830.
4. K. Javaid, W. Wu, J. Wang, J. Fang, H. Zhang, J. Gao, F. Zhuge, L. Liang and H. Cao, *ACS Photonics*, 2018, **5**, 2094-2099.
5. E. Arca, S. Lany, J. D. Perkins, C. Bartel, J. Mangum, W. Sun, A. Holder, G. Ceder, B. Gorman, G. Teeter, W. Tumas and A. Zakutayev, *Journal of the American Chemical Society*, 2018, **140**, 4293-4301.
6. W. Sun, C. Bartel, E. Arca, S. Bauers, B. Matthews, B. Orvañanos, B.-R. Chen, M. F. Toney, L. T. Schelhas, W. Tumas, J. Tate, A. Zakutayev, S. Lany, A. Holder and G. Ceder, *arXiv*, 2018, DOI: arXiv:1809.09202.
7. R. Sarmiento-Pérez, T. F. T. Cerqueira, S. Körbel, S. Botti and M. A. L. Marques, *Chemistry of Materials*, 2015, **27**, 5957-5963.
8. Y. Hinuma, T. Hatakeyama, Y. Kumagai, L. A. Burton, H. Sato, Y. Muraba, S. Iimura, H. Hiramatsu, I. Tanaka, H. Hosono and F. Oba, *Nature Communications*, 2016, **7**, 11962.
9. A. P. Jaroenjittichai and W. R. L. Lambrecht, *Physical Review B*, 2016, **94**.
10. R. Niewa and F. J. Di Salvo, *Chemistry of Materials*, 1998, **10**, 2733-2752.
11. W. Sun, A. Holder, B. Orvañanos, E. Arca, A. Zakutayev, S. Lany and G. Ceder, *Chemistry of Materials*, 2017, **29**, 6936-6946.
12. Q. Sun, W.-J. Li and Z.-W. Fu, *Solid State Sciences*, 2010, **12**, 397-403.
13. N. H. Coy and H. Sponer, *Physical Review*, 1940, **58**, 709-713.
14. T. Shiraishi, Y. Arai and S. Yamazaki, *Journal of Non-Crystalline Solids*, 1985, **77-78**, 1313-1316.
15. M. Barberon, R. Madar, M. E. Fruchart, G. Lorthioir and R. Fruchart, *Materials Research Bulletin*, 1970, **5**, 1-7.
16. K. Takenaka, T. Shibayama, D. Kasugai and T. Shimizu, *Japanese Journal of Applied Physics*, 2012, **51**, 043001.
17. E. O. Chi, W. S. Kim, N. H. Hur and D. Jung, *Solid State Communications*, 2002, **121**, 309-312.
18. F. Gabler, M. Kirchner, W. Schnelle, U. Schwarz, M. Schmitt, H. Rosner and R. Niewa, *Zeitschrift fur anorganische und allgemeine Chemie*, 2004, **630**, 2292-2298.
19. F. El Haj Hassan, *Physica Status Solidi (b)*, 2005, **242**, 3129-3137.
20. https://materials.nrel.gov).
21. S. Lany, A. N. Fioretti, P. P. Zawadzki, L. T. Schelhas, E. S. Toberer, A. Zakutayev and A. C. Tamboli, *Physical Review Materials*, 2017, **1**, 035401.
22. A. Walsh, A. A. Sokol, J. Buckeridge, D. O. Scanlon and C. R. A. Catlow, *Nature Materials*, 2018, **17**, 958-964.

23. A. C. Scheinost, A. Rossberg, D. Vantelon, I. Xifra, R. Kretzschmar, A.-K. Leuz, H. Funke and C. A. Johnson, *Geochimica et Cosmochimica Acta*, 2006, **70**, 3299-3312.
24. H. Mizoguchi, P. M. Woodward, S.-H. Byeon and J. B. Parise, *Journal of the American Chemical Society*, 2004, **126**, 3175-3184.
25. J. Li, K. Du, Y. Lai, Y. Chen and Z. Zhang, *Journal of Materials Chemistry A*, 2017, **5**, 10843-10848.
26. P. K. Sarswat and M. L. Free, *International Journal of Photoenergy*, 2013, **2013**, 1-7.
27. J. Gurgul, M. T. Rinke, I. Schellenberg and R. Pöttgen, *Solid State Sciences*, 2013, **17**, 122-127.
28. J. Pan, J. Cordell, G. J. Tucker, A. C. Tamboli, A. Zakutayev and S. Lany, *Advanced Materials*, 2019, **31**, 1807406.
29. S. Lyu, D. Skachkov, K. Kash, E. W. Blanton and W. R. L. Lambrecht, *Physica Status Solidi (a)*, 2019, 1800875.
30. S. R. Bauers, A. Holder, W. Sun, C. L. Melamed, R. Woods-Robinson, J. Mangum, J. Perkins, W. Tumas, B. Gorman, A. Tamboli, G. Ceder, S. Lany and A. Zakutayev, *arXiv: 1810.05668 [cond-mat. mtrl-sci]*, 2018.
31. S.R. Bauers, D. M. Hamann, A. Patterson, J. Perkins, K. R. Talley and A. Zakutayev, *Japanese Journal of Applied Physics*, 2019, **in press**.
32. E. Arca, A. Fioretti, S. Lany, A. C. Tamboli, G. Teeter, C. Melamed, J. Pan, K. N. Wood, E. Toberer and A. Zakutayev, *IEEE Journal of Photovoltaics*, 2018, **8**, 110-117.
33. A. N. Fioretti, A. Stokes, M. R. Young, B. Gorman, E. S. Toberer, A. C. Tamboli and A. Zakutayev, *Advanced Electronic Materials*, 2017, **3**, 1600544.
34. L. Lahourcade, N. C. Coronel, K. T. Delaney, S. K. Shukla, N. A. Spaldin and H. A. Atwater, *Advanced Materials*, 2013, **25**, 2562-2566.
35. S. Chen, P. Narang, H. A. Atwater and L.-W. Wang, *Advanced Materials*, 2014, **26**, 311-315.
36. T. Wang, C. Ni and A. Janotti, *Physical Review B*, 2017, **95**, 205205.
37. V. Stevanović, S. Lany, D. S. Ginley, W. Tumas and A. Zunger, *Physical Chemistry Chemical Physics*, 2014, **16**, 3706.
38. S. Vanka, E. Arca, S. Cheng, K. Sun, G. A. Botton, G. Teeter and Z. Mi, *Nano Letters*, 2018, **18**, 6530-6537.

Supporting Information

S1 – Theoretical predictions.

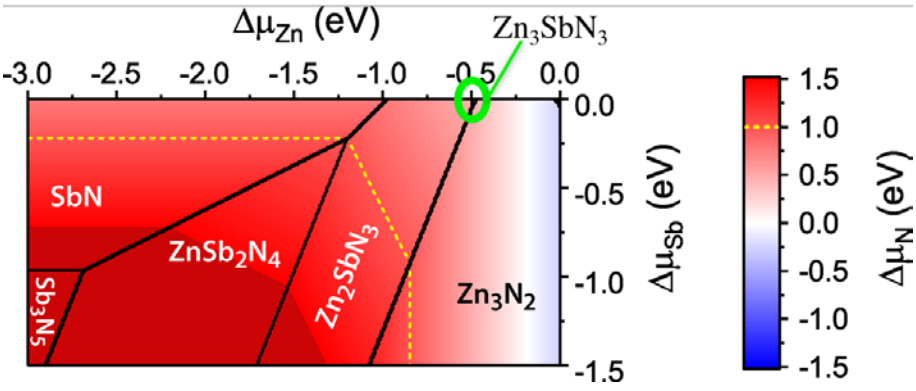

Figure SI1 Stability phase diagram of the possible Zn-Sb-N phases as determined by the KLM.

A data-mined structure prediction (DMSP) algorithm was used to identify new ternary nitrides. The stability of the candidate crystal structures was assessed by comparing their density functional theory (DFT) formation energies to the competing phases. 942 ternary metal-nitride chemical spaces were searched. Zn_2SbN_3 was identified as a candidate phase. To sample more comprehensively the Zn-Sb-N ternary space for possible compositions and their structures, we used the Kinetically Limited Minimization (KLM) approach[1]. This search was performed for many $Zn_iSb_jN_k$ chosen to accommodate the Zn^{2+}, $Sb^{3+/5+}$, and N^{3-} oxidation states. A KLM search was also performed for the Sb nitrides SbN and Sb_3N_5 which are so far unknown. As the competing phases, we considered known materials Zn_3N_2 (space group SG 206), ZnSb (SG 61), $Zn_{13}Sb_{10}$ (SG 2). The symmetry analysis for all structures was performed with the FINDSYM software[2]. The Crystallographic Information Files (CIF) were loaded

into the MAUD program to simulate the reference XRD pattern. CIF files for all new stable structures are provided as Supporting Information.

The first-principles calculations in DFT and in the GW approximation were performed with the VASP code[3, 4]. The compound enthalpy of formation was calculated using fitted elemental reference energies[5]. The GW calculations were performed as described in Ref [6] and the optical absorption spectrum was calculated within the independent particle approximation.[7]

The crystal structure predictions identified three new ternary phases in the chemical space composed by Zn, Sb and N (Figure SI1): the $ZnSb_2N_4$ phase (SG 227), Zn_2SbN_3 (SG 36) and Zn_3SbN_3 (SG 8). Additionally, a new metastable binary antimony nitride phase SbN (SG 29) is predicted. All new phases are calculated to be metastable, as they require a highly activated Nitrogen source with chemical potentials well above the thermodynamic N_2 gas phase. Effective N chemical potential up to about $\Delta\mu N \approx 1$ eV above the low-temperature limit of N_2 have been demonstrated before by sputtering deposition[8]. The trivalent Sb nitride SbN becomes stable at $\Delta\mu N \geq +0.8$ eV, and, thus, might be synthesizable (efforts towards synthesis of SbN are ongoing and will be reported elsewhere). However, the pentavalent Sb_3N_5 requires $\Delta\mu N \geq +1.7$ eV and is likely out of reach, even for nonequilibrium thin-film synthesis.

As seen in the phase diagram in Fig. 1A, the spinel phase $ZnSb_2N_4$ shows a wide stability region among the ternary Zn-Sb nitrides. However, it requires very high $\Delta\mu N$, $\geq +1.0$ eV, across its entire space, suggesting that synthesis would be difficult, if possible at all. Thus, it could be challenging to synthesize it as phase-pure material. It is noticeable that the addition of Zn in the ternary strongly stabilizes the Sb +5 oxidation

state, which is highly unstable as a binary Sb nitride. The relative stability of Zn_2SbN_3 also practically eliminates in the phase diagram the presence of ternary nitrides with Sb in the +3 state. Even though the third phase, Zn_3SbN_3 with Sb in the +3 state, has a similar critical $\Delta\mu N$, it has a very small stability window between Zn_2SbN_3, Zn_3N_2, and elemental Sb.

S2 – Experimental synthesis and characterization.

Experimental synthesis of Zn-Sb-N thin-film sample libraries was performed using combinatorial co-sputtering of Zn and Sb metals in the presence of N_2 on glass substrates in a deposition chamber with base pressure better than 1×10^{-6} Torr. Two sputtering guns were loaded with 2"-diameter Zn and Sb metal targets and positioned at 45° with respect to the substrate normal to achieve a cation compositional gradient. Both temperature and sputtering powers were varied to assess the effect of the deposition conditions on the properties of Zn_2SbN_3. Before the deposition, the 2"×2" Eagle-XG glass substrates were cleaned by degreasing in water and soap, followed by ultrasonic cleaning in acetone and isopropanol baths. The flow of the gases was set to 10 and 10 sccm for Ar and N_2, respectively. The sputtering pressure was adjusted between 20 and 10 mTorr, to change from more nitridizing to more reducing conditions during the growth.

Spatially resolved characterization of the thin-film sample libraries was performed on a 4×11 grid of samples - 4 rows and 11 columns, with the compositional gradient along the 11 positions in one row. Compositional analysis was performed by both X-Ray

Fluoresce in combinatorial mode and by Rutherford Back Scattering (RBS) on selected samples. For XRF, a Fischer Scientific (Fischerscope XDV-SDD) instrument using a spot size of 3 mm in diameter was used. Rutherford backscattering was performed using a model 3S-MR10 RBS system from National Electrostatics Corporation, with either high (168°, RBS) or low (110°, RBG) scattering angles. More information about the technique can be find elsewhere[1].

Structural characterization was performed using a Bruker D8 XRD in Cu Kα radiation, equipped with a two-dimensional (2-D) detector and a spot size on the order of 2 mm × 3 mm. For selected samples Structural characterization was performed using Beamline 11-3 at the Stanford Synchrotron Radiation Lightsource (SSRL) with an incident wavelength of 0.9744 Å. The experimental data were collected by using a Rayonics 225 2D detector and the data range is 0.52 Å-1 ≤ q ≤ 5.40 Å-1. q was obtained by using the equation $q = \frac{4\pi}{\lambda}\sin\theta$, where λ is the incident wave length and θ is the diffraction angle. The integration and background removal were performed by using GSAS-II software.[9]

The optical transmittance and reflectance were measured in the wavelength range of 300−1700 nm on a home-built ultraviolet−visible light−near-infrared (UV-vis-NIR) spectrometer (no integrating sphere) with a spot diameter of ~1 mm. Electrical conductivity was measured using a custom four-point probe measurement instrument with tungsten probe spacing of 1 mm. The analysis of the characterization results was performed using custom-written procedures in the Wavemetrics IGOR Pro software package. The resulting data are available at htem.nrel.gov.

X-Ray Photoelectron Spectroscopy (XPS) and Ultraviolet Photoelectron Spectroscopy (UPS) was performed using a PHY-5600 system. A monochromatic Al k-alpha source was employed for the XPS measurements whereas a He(I) line was used for the UPS measurements.

XRD pattern as a function of cation composition plotted heat maps are reported in SI2, for some selected deposition conditions tested. As it can be seen, the crystallinity region is more extended for sample grown at 20 mTorr and at moderate temperature (200°C).

T_{dep} = RT

P_{dep} = 10mTorr

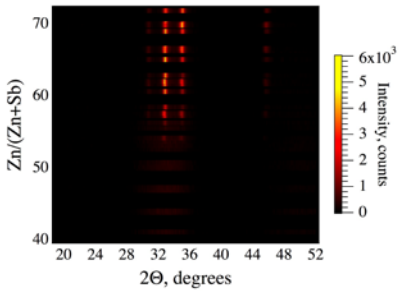

P_{dep} = 20mTorr

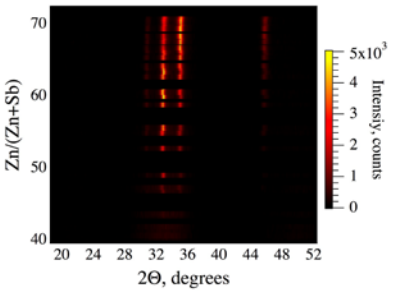

T_{dep}=200°C

P_{dep} = 10mTorr

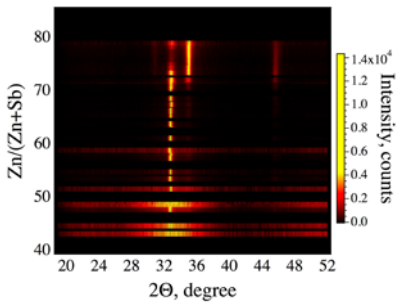

P_{dep} = 15mTorr

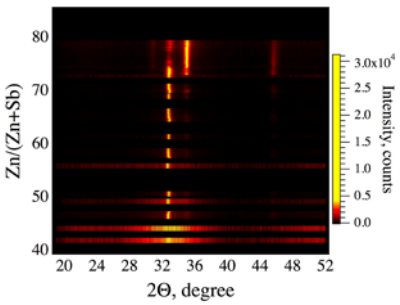

P_{dep} = 20mTorr

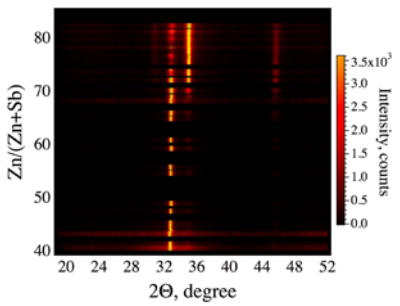

T_{dep}=300°C
P_{dep} = 20mTorr

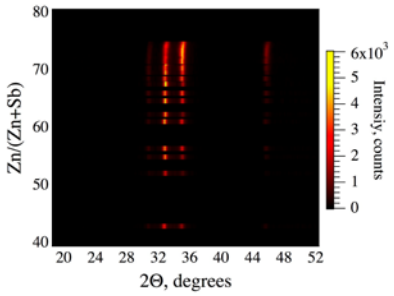

Figure SI 2. XRD patterns reported as heat maps for several deposition conditions tested

Table 1. Comparison between the cation composition determined by RBS and the XRF for a selected point in the library. The first two points (Row1-Column1, Row1-Column3 in the map where the columns are numbered 0 to 10) are composition outside of the crystallinity region.

Position	f_{Zn} RBS	f_{Zn} XRF	Full stoichiometry	Crystalline/Amorphous
R1C1	0.31	0.30	$Zn_{0.9}Sb_2N_{2.5}$	Amorphous
R1C3	0.35	0.37	$Zn_{1.1}Sb_2N_{3.4}O_{0.03}$	Amorphous
R1C5	0.63	0.65	$Zn_{1.7}SbN_3O_{0.28}$	Crystalline
R1C7	0.71	0.71	$Zn_{2.5}SbN_{3.7}$	Crystalline
R1C9	0.73	0.74	$Zn_{2.7}SbN_{3.8}$	Crystalline

The first two points were acquired in a portion of the sample which was Sb-reach, outside the crystallinity region identified by XRD. Thus, they refer to a part of the sample which was amorphous. The last three points were acquired at composition within the crystallinity range. The change from amorphous to crystalline is also accompanied with a drastic change in the elemental ratio, particularly the Zn/N content.

Selected samples were subject to RBS measurements to determine the nitrogen and oxygen content in the films and compared the cation composition determined by XRF with the value determined by RBS. Table S1 reports the values for one specific library where RBS was conducted on a spatially resolved manner. This analysis shows that the XRF determined values of cation composition were very accurate (within 1% of the values determined by RBS). Oxygen content in the films was very low, and it could be detected above the background signal only for few points in the sample. This is conducive of the that the oxygen content in the film is below 10%.

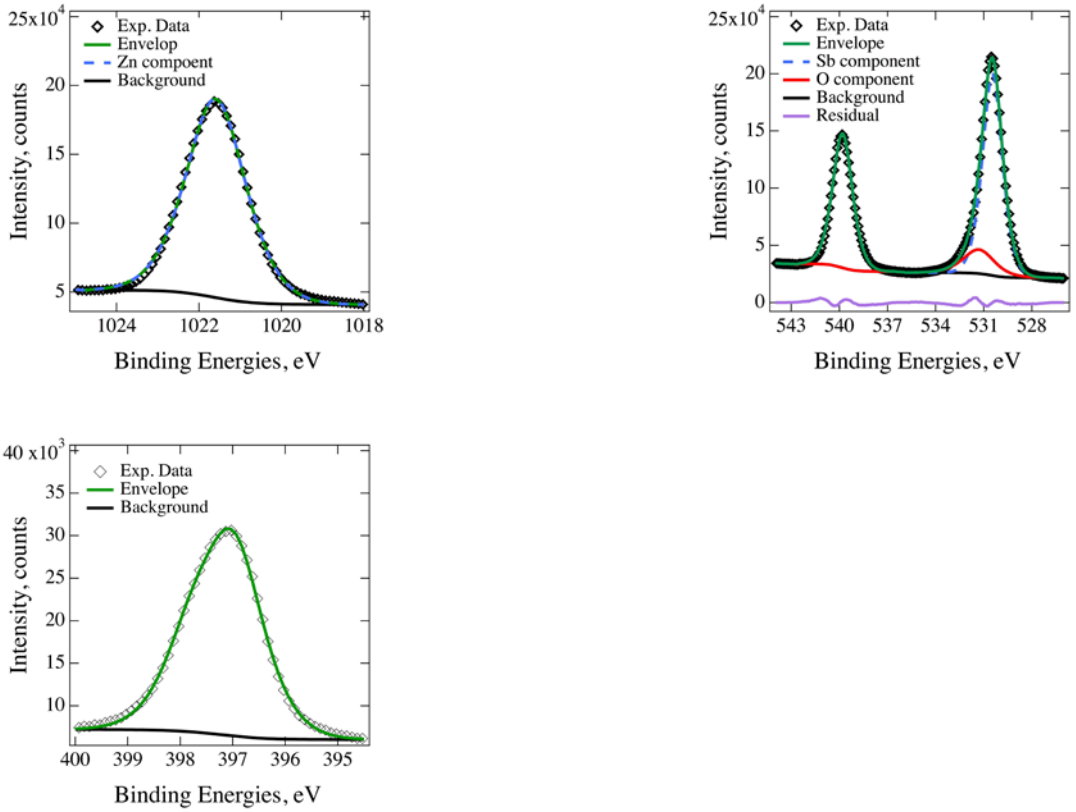

Figure SI 3. Core levels recorded for Zn, O and N respectively.

Figure SI3 reports the XPS spectra recorded on a film grown at room temperature and having composition f_{Zn} =0.65. The Zn $2p_{3/2}$, Sb 3d and N1s core levels are reported here. The $Sb3d_{5/2}$ core level of antimony is superimposed with the O 1s level. In order to separate the related contribution, peak fitting on the Sb 3d peaks was carried out using a tabulated spin orbit splitting separation between the Sb $3d_{5/2}$ and $3d_{3/2}$ and the ratio between the integrated area of 3:2. The residual on the peak positioned at ~531eV was fitted with a single component which is attributed to the O1s contribution. In order to assess whether $Zn(OH)_2$ was present at the surface, Zn-Auger lines were acquired during the survey. Based on the position of the Zn 2p core-level and the position of the

Auger lines (Auger KE = 988.8 eV), we ruled out the presence of $Zn(OH)_2$ at the surface, however we cannot rule out the presence of a very small amount of ZnO.

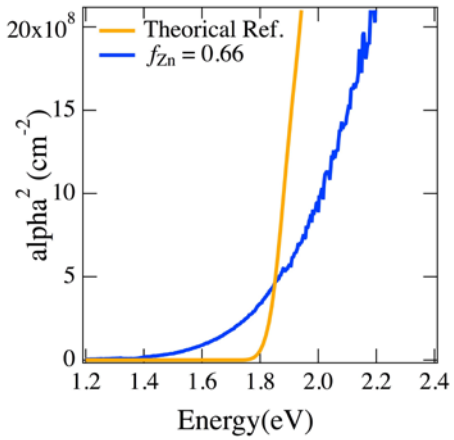

Figure SI 4. Squared value of the absorption coefficient plotted as a function of energy.

Optical spectra for a nearly stoichiometric films were recorded. In order to determine the position of the absorption onset, the absorption coefficient was plotted as squared function. For comparison the theoretical spectrum is reported as well. Whereas theory predicts a fundamental direct band gap of 1.71 eV, the absorption onset of these films is slightly more diffused and start at lower energies. This behavior has been observed in other materials which adopt the wurtzite derived structure and it is attributed to disorder on the cation sublattice.

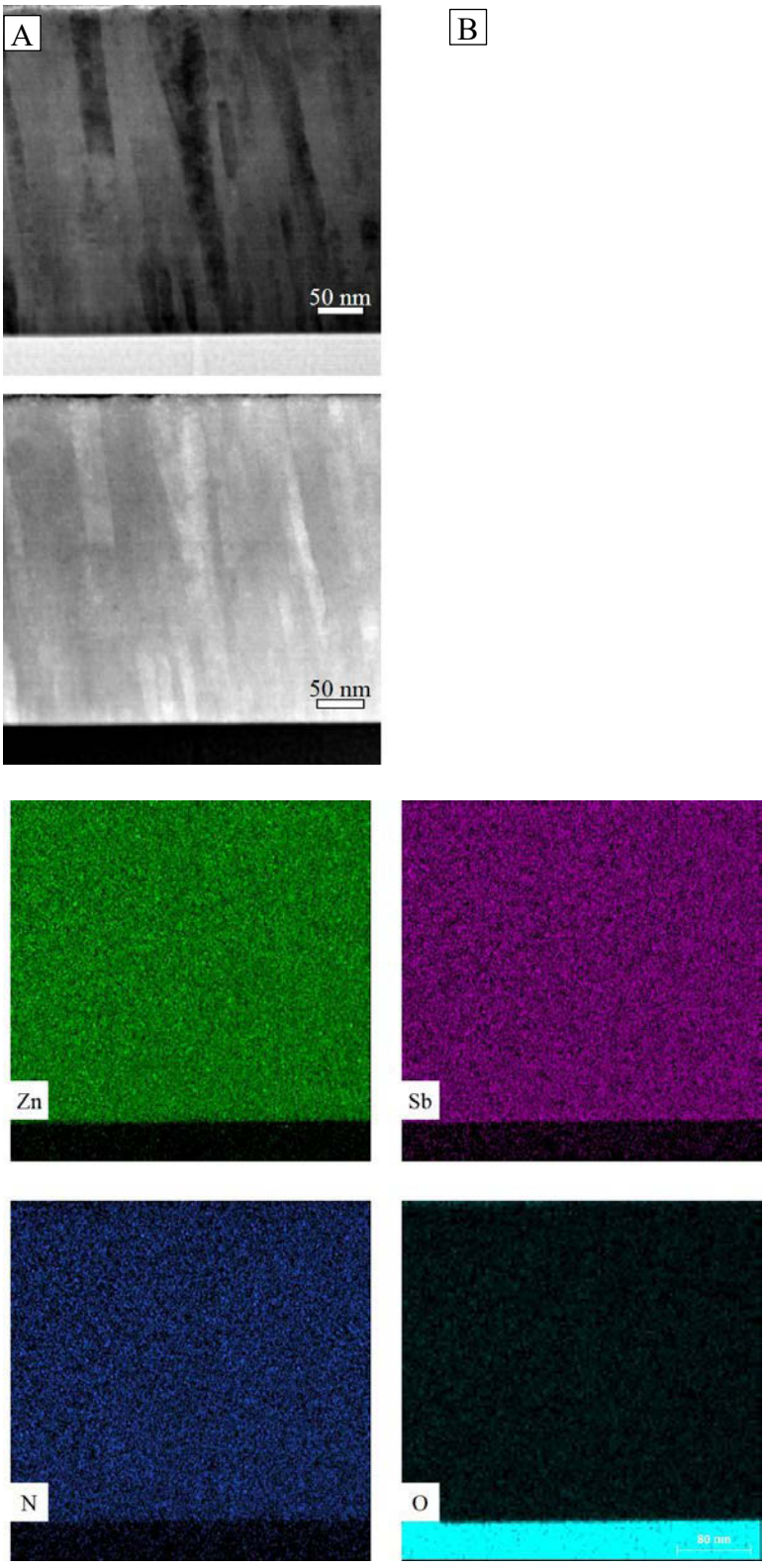

Figure SI 5. A) TEM and B) EDX mapping of a sample grown at room temperature.

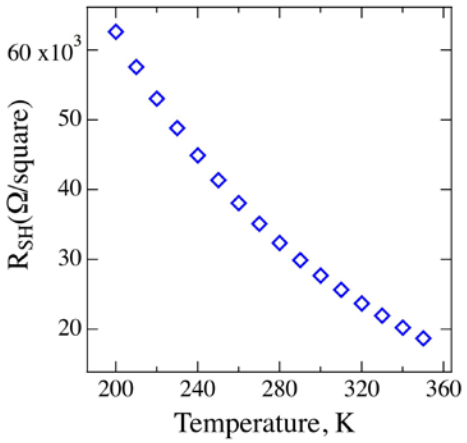

Figure SI 6. Sheet resistance measured as a function of temperature.

An example of the resistance vs temperature measurements is reported in Figure SI6. The temperature activated behavior indicates that Zn_2SbN_3 is a semiconductor.

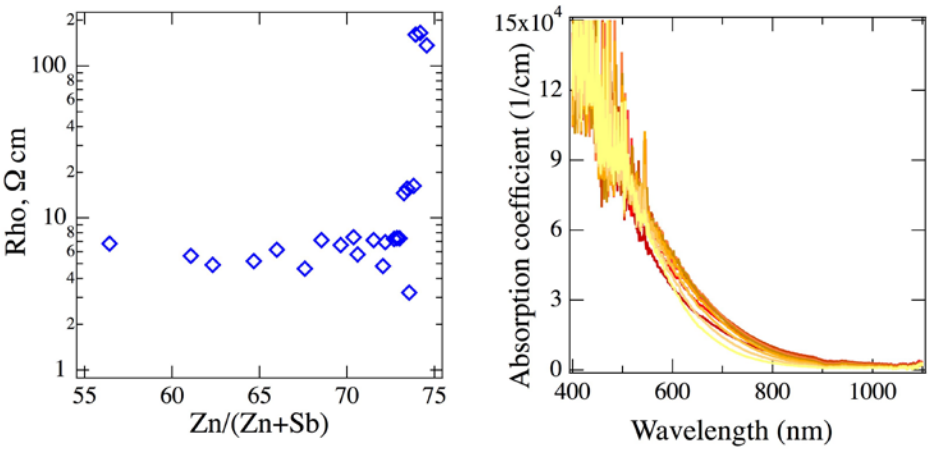

Figure SI 7 A) Resistivity and B) Absorption coefficient reported as a function of composition.

Figure SI7A reports the electrical measurements of two thin films measured grown at different substrate temperature as a function of composition: unintentional heat (RT

temperature) and substrate temperature of 300°C. The resistivity of the sample increases substantially at the edge of the crystallinity region, having very small variation with composition within the crystallinity region and decreasing for samples deposited at moderate temperature. The absorption coefficient remains quite unchanged in the composition region spanning from f_{Zn} =0.8 to f_{Zn} =0.65

References

1. E. Arca, S. Lany, J. D. Perkins, C. Bartel, J. Mangum, W. Sun, A. Holder, G. Ceder, B. Gorman, G. Teeter, W. Tumas and A. Zakutayev, *Journal of the American Chemical Society*, 2018, **140**, 4293-4301.
2. H. T. Stokes and D. M. Hatch, *Journal of Applied Crystallography*, 2005, **38**, 237-238.
3. G. Kresse and D. Joubert, *Physical Review B*, 1999, **59**, 1758-1775.
4. M. Shishkin and G. Kresse, *Physical Review B*, 2006, **74**, 035101.
5. V. Stevanović, S. Lany, X. Zhang and A. Zunger, *Physical Review B*, 2012, **85**, 115104.
6. S. Lany, *Physical Review B*, 2013, **87**, 085112.
7. M. Gajdoš, K. Hummer, G. Kresse, J. Furthmüller and F. Bechstedt, *Physical Review B*, 2006, **73**, 045112.
8. C. M. Caskey, R. M. Richards, D. S. Ginley and A. Zakutayev, *Materials Horizons*, 2014, **1**, 424-430.
9. B. H. Toby and R. B. Von Dreele, *Journal of Applied Crystallography*, 2013, **46**, 544-549.